THE JOURNAL OF PHYSICAL CHEMISTRY C

Article

pubs.acs.org/JPCC

RuO_2 Monolayer: A Promising Bifunctional Catalytic Material for Nonaqueous Lithium−Oxygen Batteries

Le Shi, Ao Xu, and Tianshou Zhao*

Department of Mechanical and Aerospace Engineering, The Hong Kong University of Science and Technology, Clear Water Bay, Kowloon, Hong Kong SAR, China

Supporting Information

ABSTRACT: Rutile RuO_2 has been widely regarded as an excellent catalyst for the oxygen reduction reaction (ORR) and oxygen evolution reaction (OER) in nonaqueous lithium−oxygen batteries and achieved superior performance, but the catalytic activity of RuO_2's polymorph, RuO_2 monolayer, has been less studied. In this work, we study the catalytic activities of both rutile RuO_2 and RuO_2 monolayer for ORR and OER in the battery using density functional theory method. Computational results show that the RuO_2 monolayer exhibits a higher catalytic activity than the rutile RuO_2 does. More interestingly, it is found that during discharge a similar lattice structure between RuO_2 monolayer and Li_2O_2 {0001} surface can induce the formation of crystallized Li_2O_2 with the conductive {0001} surface exposed, whereas during charge the RuO_2 monolayer can attract the remaining Li_2O_2 to its surface spontaneously, thus maintaining the solid−solid reaction interface. Our results suggest that the RuO_2 monolayer is a promising catalytic material for nonaqueous lithium−oxygen batteries.

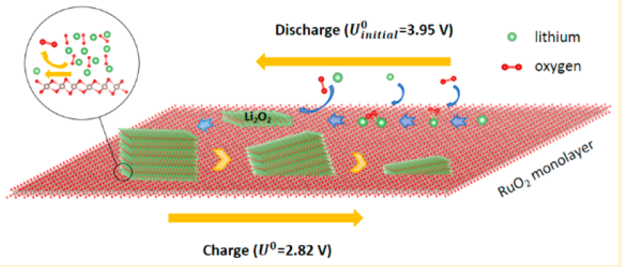

1. INTRODUCTION

Nonaqueous lithium−oxygen batteries have attracted increasing attention because of their superhigh specific capacities;[1−7] however, as an infant stage technology, this novel energy-storage system is still suffering from several severe issues, such as the high charge overpotential, sluggish reaction kinetics, and poor cycling stability, which seriously hindered its commercialization. A common strategy to solve these issues is using catalyst to lower the charge overpotential and accelerate the reactions, which could also alleviate the decomposition of electrolyte and cathode materials, thus enhancing cycling stability. Many possible catalysts have been tested,[8−14] among which rutile RuO_2 is a popular candidate for its superior catalytic activity and good chemical stability in the highly oxidative environment of nonaqueous lithium−oxygen batteries.[15−17] As the polymorph of rutile RuO_2, RuO_2 monolayer exfoliated from lamellar ruthenates is also conductive and has been used as super capacitor and catalyst for the oxygen reduction reaction (ORR) in aqueous system.[18−21] Being a 2D metal oxide, RuO_2 monolayer can achieve a large surface-to-mass ratio and exist stably during the operation of nonaqueous lithium−oxygen batteries. It is also expected to catalyze the reactions uniformly without the necessity to introduce defects or functional groups as carbon material does, making it a possible candidate for the catalyst or catalytic cathode of nonaqueous lithium−oxygen batteries. Recently, Liao et al.[22] used lamellar ruthenate as a precursor to obtain RuO_2 nanosheet to be a catalytic cathode of nonaqueous lithium−oxygen batteries and achieved excellent performance. In their experiment, however, a considerable amount of exfoliated RuO_2 monolayer went through phase change and turned to rutile RuO_2 during the heat treatment process. Thus, whether RuO_2 monolayer contributed to the excellent performance is still unclear. Further detailed computational and experimental investigations are needed to identify whether RuO_2 monolayer is a promising effective catalytic material for nonaqueous lithium−oxygen batteries.

In this work, using density functional theory (DFT) method, we investigated the catalytic activities of both rutile RuO_2 and RuO_2 monolayer for the ORR and oxygen evolution reaction (OER) in nonaqueous lithium−oxygen batteries. The dominant surface of rutile RuO_2 was identified according to the Wullf construction to be representative in the study of the catalytic activity of rutile RuO_2. The adsorption behaviors of the lithium ion, intermediate discharge product LiO_2, and discharge product Li_2O_2 on both RuO_2 monolayer and the dominant surface of rutile RuO_2 were investigated to study the initial discharge process. The electronic properties of RuO_2 monolayer before and after the deposition of different layers of Li_2O_2 were obtained to study the following discharge process when Li_2O_2 accumulates after the initial deposition. Interfacial models among RuO_2 monolayer or the dominant surface of rutile RuO_2, Li_2O_2, and electrolyte were built to study the charge process.

2. COMPUTATIONAL DETAILS

DFT calculations were performed using the ABINIT[23−25] software package with the projector-augmented-wave (PAW)

Received: January 4, 2016
Revised: March 3, 2016
Published: March 9, 2016

DOI: 10.1021/acs.jpcc.6b00014
J. Phys. Chem. C 2016, 120, 6356−6362

method[26] and Perdew–Burke–Ernzerhof (PBE) generalized gradient approximation (GGA).[27] The cutoff energy for the plane-wave basis was 20 Ha. Monkhorst–Pack scheme[28] was used for the k-point sampling, and the spacing of the k-point mesh was set to be <0.05 $Å^{-1}$. All atoms were relaxed to a force tolerance of 0.02 eV $Å^{-1}$ or less for the geometric optimization. The Bader charge partition analysis[29,30] implemented in the ABINIT software was employed to study the related charge transfer. The density of states (DOS) were calculated using Heyd–Scuseria–Ernzerhof (HSE) hybrid density functional[31,32] implemented in Quantum Espresso package.[33] One-quarter (α = 0.25) of the local DFT exchange was replaced by the unscreened and nonlocal Fock exchange.

The crystal structure of RuO_2 monolayer was obtained by modifying the crystal structure of $Na_xRuO_2{\cdot}yH_2O$.[34] The optimized lattice parameters of RuO_2 monolayer (listed in Table S1) agree well with experimental reports.[19] The crystal structure of rutile RuO_2 and Li_2O_2 was taken from experimental results.[35,36]

Slab model adding vacuum layers was used to calculate the surface energies. All slabs are symmetrized and contain more than seven repeating layers with a vacuum layer thicker than 10 Å to achieve convergence within 1 meV $Å^{-2}$ for the surface energies. The surface energies were calculated by

$$\gamma = \frac{1}{2A}[G_{slab} - N_{Ru}\mu_{Ru}^{bulk} - N_O\mu_O^{bulk}] \quad (1)$$

where A is the slab surface area, G_{slab} is the total free energy of the slab supercell, N_{Ru} and N_O are the numbers of ruthenium and oxygen atoms, and μ_{Ru}^{bulk} and μ_O^{bulk} are the chemical potentials of ruthenium and oxygen atoms, respectively. The chemical potentials of RuO_2 are correlated by

$$\mu_{Ru}^{bulk} + 2\mu_O^{bulk} = G_{RuO_2} \quad (2)$$

Thus the surface energies can be rewritten as

$$\gamma = \frac{1}{2A}[G_{slab} - N_{Ru}G_{RuO_2} + (2N_{Ru} - N_O)\mu_O^{bulk}] \quad (3)$$

The Wulff shape was constructed using the WinXmorph software.[37]

A 3 × 3 supercell of RuO_2 monolayer and a 2 × 2 supercell of rutile RuO_2 {001} surface with a 15 Å vacuum layer were used to study the adsorption behavior. For the rutile RuO_2 {001} surface, the two exposed surfaces are kept symmetrically equivalent for all calculations to eliminate the polarization effect. For LiO_2 and Li_2O_2, the adsorption energies were calculated using

$$E_{ads} = E_{tot}(S + A) - E_{tot}(A) - E_{tot}(S) \quad (4)$$

where E_{tot}(S+A) is the total energy of the adsorbed substrate, E_{tot}(A) is the total energy of adsorbate, and E_{tot}(S) is the total energy of substrate. For $Li^+ + e^-$, the adsorption energy was calculated by

$$E_{ads} = E_{tot}(S + A) - E_{tot}(S) - \mu_{Li} \quad (5)$$

where μ_{Li} is equal to the chemical potential of bulk lithium.

To address the well-known oxygen overbinding issue in DFT calculations, we calculated the enthalpy of oxygen molecule using[38]

$$H(T = 0\ K, O_2) = 2H(T = 0\ K, O) - \Delta E^{exptl} \quad (6)$$

where $H(T = 0\ K)$ is the calculated zero-point energy of oxygen atom or molecule and ΔE^{exptl} (5.12 eV)[38] is the binding energy of oxygen from experiments. The chemical potential of oxygen was calculated by

$$\mu_{O_2}(T, P_{O_2}) = H_{O_2}(0\ K) + \Delta H_{O_2}(T) - TS_{O_2}^{exptl}(T) + k_BT\ \ln\left(\frac{P_{O_2}}{P_{O_2}^0}\right) \quad (7)$$

where $\Delta H_{O_2}(T)$ is the enthalpy energy change from 0 K to T, for which we used diatomic ideal gas approximation as $7/2k_BT$, and $S_{O_2}^{exptl}(T)$ is the entropy of oxygen at 1 atm and different temperatures obtained from experiments.[39] $P_{O_2}^0$ is set to be 1 atm.

The energy profiles of the ORR/OER process were calculated by adding/removing a lithium atom or an oxygen molecule at each step. The reaction free energy of intermediate steps was calculated by

$$\Delta G = E - E_0 + \Delta N_{Li}(\mu_{Li} - eU) + \Delta N_{O_2}\mu_{O_2} \quad (8)$$

where E is the total energy of the considered slab model, E_0 is the total energy of the initial slab model, ΔN_{Li} and ΔN_{O_2} are the numbers of lithium atoms and oxygen molecules added/removed for each step, and μ_{Li} and μ_{O_2} are the chemical potentials of lithium bulk and oxygen, respectively. The eU term was added to account for the electronic energy under applied potential U. The overpotential was defined by shifting all intermediates to $\Delta G < 0$, which is consistent with previous works.[40–42]

3. RESULTS AND DISCUSSION

3.1. Representative Surface of Rutile RuO_2. To identify the stable surfaces of rutile RuO_2 in the operation condition of nonaqueous lithium–oxygen batteries, we calculated the surface energies of {001}, {100}, {101}, {110}, and {111} surfaces with different terminations (as shown in Figure S1). The calculated surface energies under different oxygen chemical potentials are shown in Figure 1a. Because nonaqueous lithium–oxygen batteries operate in an oxygen-rich condition, here we take the surface energies when P_{O_2} = 1 atm to construct the Wulff structure of rutile RuO_2. From the Wulff shape shown in Figure 1b, it can be found that the {001} surface occupies most of the

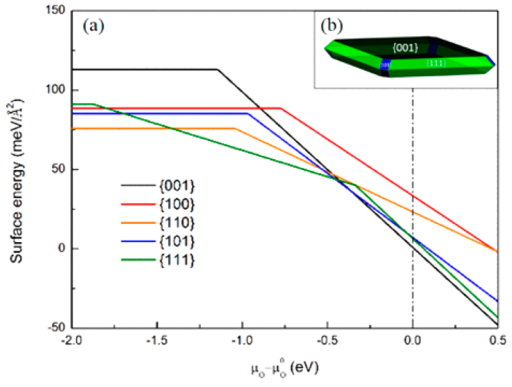

Figure 1. (a) Surface energies of rutile RuO_2 at different oxygen chemical potentials and (b) the Wulff construction of rutile RuO_2 when $P(O_2)$ = 1 atm.

DOI: 10.1021/acs.jpcc.6b00014
J. Phys. Chem. C 2016, 120, 6356–6362

Table 1. Adsorption of $Li^+ + e^-$, LiO_2, and Li_2O_2 onto the RuO_2 Monolayer and Rutile RuO_2 {001} Surface, Respectively

	E_{ads} (eV)		D_{O-O} (Å)		δ(e) of adsorbate	
adsorbate	RuO_2 monolayer	RuO_2{001}	RuO_2 monolayer	RuO_2{001}	RuO_2 monolayer	RuO_2{001}
$Li^+ + e^-$	−5.27	−3.67	–		+0.91	+0.88
LiO_2	−4.18	−2.21	1.27	1.24	+0.55	+0.78
Li_2O_2	−5.02	−3.29	1.37	1.27	+0.91	+1.44

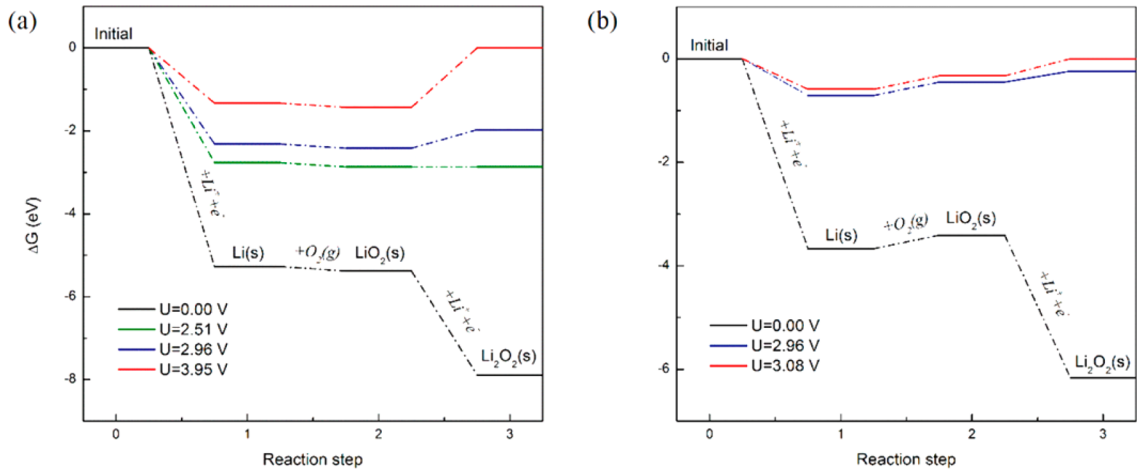

Figure 2. Energy profiles for the initial discharge process happened on (a) the surface of RuO_2 monolayer and (b) rutile RuO_2 {001} surface.

exposed surface area. Thus, in the following, we will take the {001} surface as a representative of rutile RuO_2 to study its catalytic activities toward the ORR and OER in nonaqueous lithium−oxygen batteries.

3.2. Initial Discharge Process on RuO_2 {001} and RuO_2 Monolayer. It is now widely agreed that the ORR in nonaqueous lithium−oxygen batteries goes through a two-step reaction.[1−6] In the first step, the oxygen molecular will complex with a lithium ion and get an electron to form lithium superoxide as

$$Li^+ + O_2 + e^- \rightarrow LiO_2 \qquad \text{(step 1)}$$

Then, the formed LiO_2 could either go through an electrochemical reaction route and be further reduced to Li_2O_2 as

$$LiO_2 + Li^+ + e^- \rightarrow Li_2O_2 \qquad \text{(step 2.1)}$$

or go through a chemical disproportionation reaction route as

$$2LiO_2 \rightarrow Li_2O_2 + O_2 \qquad \text{(step 2.2)}$$

The electrochemical reactions take place only on the catalytic surfaces, whereas the chemical disproportionation reaction can happen anywhere. It is commonly believed that the large compact toroid Li_2O_2 particles resulted from the chemical disproportionation reactions that happened in electrolyte.[43,44] From our calculation results on the adsorption behaviors of $Li^+ + e^-$, LiO_2, and Li_2O_2 onto both RuO_2 monolayer and rutile RuO_2 {001} surface, as listed in Table 1, it can be found that in the both cases the adsorption energies of LiO_2 are quite large. The large adsorption energies of LiO_2 could confine all reactions onto the surfaces in the initial stage of discharge process, rather than letting the LiO_2 dissolve into the electrolyte and disproportionate into Li_2O_2, thus effectively suppressing the formation of large compact toroid particles that are hard to be charged back.[45] So, in this study, we only consider the disproportionation reactions that happened on the surfaces.

The detailed reaction route for the disproportionation reaction occurring on the surfaces can be much more complex. Here we consider only the reaction enthalpy change for an initial evaluation by defining the formation heat following Geng et al.'s[45] approach as

$$E_{dis} = E_{Li_2O_2@surf} - 2E_{LiO_2@surf} + E_{surf} + E_{O_2} \qquad (9)$$

where E_{O_2}, E_{surf}, $E_{LiO_2@surf}$, and $E_{Li_2O_2@surf}$ represent the energy of oxygen molecule, considered surface, considered surface adsorbed with LiO_2, and considered surface adsorbed with Li_2O_2, respectively. The calculated E_{dis} for the disproportionation reactions that happened on the RuO_2 monolayer is +3.17 eV, and for the rutile RuO_2 {001} surface it is +0.953 eV, which means the disproportionation reactions on both surfaces are endothermic and can hardly be realized.

We now discuss the electrochemical route. As for both the RuO_2 monolayer and rutile RuO_2 {001}, all ruthenium atoms are coordinatively saturated, making the initial adsorption of oxygen not preferred, which can be further confirmed by the bond lengths of adsorbed oxygen molecules onto the surfaces, as shown in Figures S3 and S4. Thus, we study the electrochemical ORR in nonaqueous lithium−oxygen batteries by taking the reaction route Li → LiO_2 → Li_2O_2. The corresponding energy profiles for this process on different surfaces are shown in Figure 2. For both RuO_2 monolayer and rutile RuO_2 {001} surface, the ORR following the electrochemical reaction route are thermodynamically favored. Figure 2a shows the energy profiles of the ORR on the RuO_2 monolayer at an open-circuit potential (U = 0 V), the highest voltage at which discharging is energetically downhill for all steps (U = 2.51 V), the equilibrium voltage of bulk Li_2O_2 (U = 2.96 V),[39] and the equilibrium voltage for the initial discharge process, which could just keep all of the intermediates having a negative energy (U = 3.95 V). Figure 2b presents the energy profiles of the ORR on the rutile RuO_2 {001} surface at an open-circuit potential (U = 0 V), the equilibrium voltage of

DOI: 10.1021/acs.jpcc.6b00014
J. Phys. Chem. C 2016, 120, 6356−6362

bulk Li_2O_2 (U = 2.96 V),[39] and the equilibrium voltage for the initial discharge process, which could just keep all of the intermediates having a negative energy (U = 3.08 V). It can be found that the equilibrium voltage for the electrochemical ORR on RuO_2 monolayer is as high as 3.95 V, much higher than that of the equilibrium voltage on rutile RuO_2 {001} (3.08 V), indicating a higher catalytic activity of RuO_2 monolayer toward the electrochemical ORR process. This result may also explain the experimental discharge curve of Liao et al., where an initial discharge voltage higher than 3.5 V was observed (corresponding to the equilibrium voltage as high as 3.95 V in the initial stage of the discharge process) and gradually drop down to a voltage plateau below 2.96 V (corresponding to the equilibrium voltage of the following discharge process that happened on Li_2O_2 surface after RuO_2 monolayer surface was fully covered by discharge product).[22] The reverse process of the initial discharge process is the charge process in its final stage, when there is only a very small number of Li_2O_2 molecules adsorbed onto the surfaces waiting to be removed, corresponding to a high ending charge voltage for RuO_2 monolayer, which also agrees with the experimental observation.[22] The geometry change along with the initial discharge process on the surfaces is shown in Figure 3.

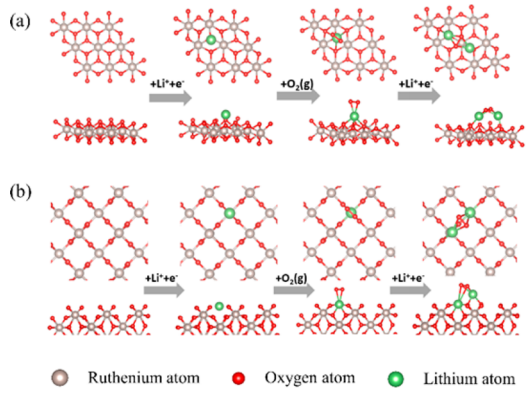

Figure 3. Geometries for the initial discharge process happened on (a) the surface of RuO_2 monolayer and (b) rutile RuO_2 {001} surface.

3.3. Electronic Conductance of RuO_2 Monolayer Deposited with Li_2O_2. As the discharge goes on, the active surfaces will be covered by Li_2O_2 and show little influence toward the following discharge process (shown in Figures S5 and S6). From the results of our previous work,[46] the surface of Li_2O_2 also has a strong adsorption ability toward LiO_2, and thus the following ORR reactions will mainly take place at the surfaces of Li_2O_2. Because Li_2O_2 bulk is insulator, the electronic conductivity of Li_2O_2 will become the main limiting factor for the following ORR.[1−6] For rutile RuO_2, its lattice structure and lattice parameters are quite different from those of Li_2O_2, which could induce the formation of amorphous Li_2O_2 and increase the electronic conductivity through the formation of grain boundaries.[15,45]

For RuO_2 monolayer, it should be noted that the crystal structures of Li_2O_2 {0001} surface and RuO_2 monolayer are similar, and their lattice parameters are quite close, as listed in Table S1. Considering that lithium atoms tend to adsorb onto the hcp hollows formed by the Ru atoms (shown in Figure 3a) and {0001} surface is the dominant surface of Li_2O_2 in its equilibrium Wulff structure,[38,42,47] we propose that after the initial deposition process the formed Li_2O_2 is very likely to adsorb onto the surface of RuO_2 monolayer in the way shown in Figure 4. In this way, the optimized lattice parameters of Li_2O_2 after adsorbed onto RuO_2 monolayer are quite close to that of bulk Li_2O_2 (as shown in Figure S7).

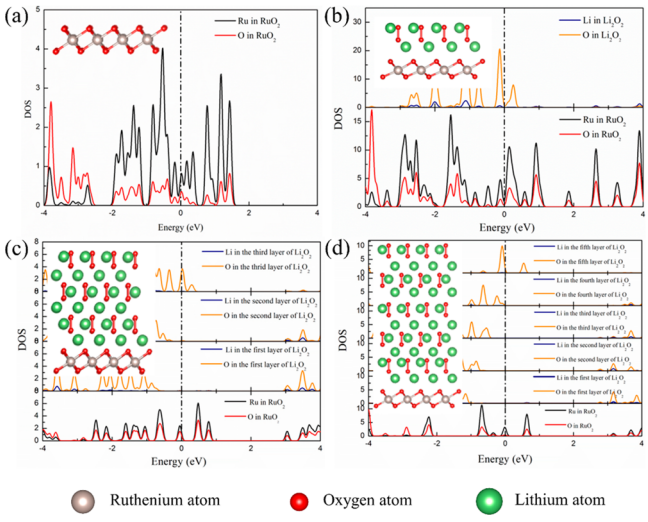

Figure 4. Density of states (DOS) map for the RuO_2 monolayer before (a) and after deposition of one (b), three (c), and five (d) layers of Li_2O_2.

We now present the study on electronic conductivity of RuO_2 before and after the deposition of one, three, and five layers of Li_2O_2. HSE hybrid density functional was used to get accurate band information.[31,32] The constructed models and calculated DOS maps are shown in Figure 4. According to the calculation results, RuO_2 monolayer is a metallic material (Figure 4a), which is consistent with experimental observations.[18−21] After the deposition of one layer of Li_2O_2, the RuO_2 monolayer and the deposited Li_2O_2 are both conductive (Figure 4b). If we continue to increase the Li_2O_2 deposition (Figures 4c,d), the RuO_2 monolayer will still be conductive, while the conductive Li_2O_2 layer will shift up to the top layer exposed, which will be further away from RuO_2. At the same time, the Li_2O_2 layer in contact with the RuO_2 monolayer will exhibit to be an insulator with a band gap larger than 4.0 V, which is similar to that of bulk Li_2O_2.[48,49] This phenomenon is consistent with the previous result that the {0001} surface of Li_2O_2 is conductive.[38] The surface conductivity would provide an electron pathway for the following discharge process.

Because a small lattice mismatch between Li_2O_2 and RuO_2 monolayer exists, the strain caused by lattice mismatch will become larger as the adsorbed Li_2O_2 grows thicker.[50] This strain may induce the generation of defects and grain boundaries, which could further enhance the electronic conductivity.[49,51] The {111} surface of previously reported cathode material for nonaqueous lithium−oxygen batteries, TiC, also has s similar lattice structure and a small lattice mismatch compared with the Li_2O_2 {0001} surface.[52] It is quite interesting to notice that the discharge product morphologies on TiC cathode[53] and RuO_2 nanosheet cathode[22] are also similar; in both cases, a rare morphology of assembled thin discs was observed. We propose that this morphology may be caused by the stripping of Li_2O_2 along the {0001} surface to relieve the internal strain, as shown in Figure S8, just as those observed in heteroeptaxial growth experiments.[50,54,55]

3.4. Charge Process on Rutile RuO_2 {001} and RuO_2 Monolayer. The involvement of solid-state discharge product makes the ORR and OER in nonaqueous lithium−oxygen

DOI: 10.1021/acs.jpcc.6b00014
J. Phys. Chem. C 2016, 120, 6356−6362

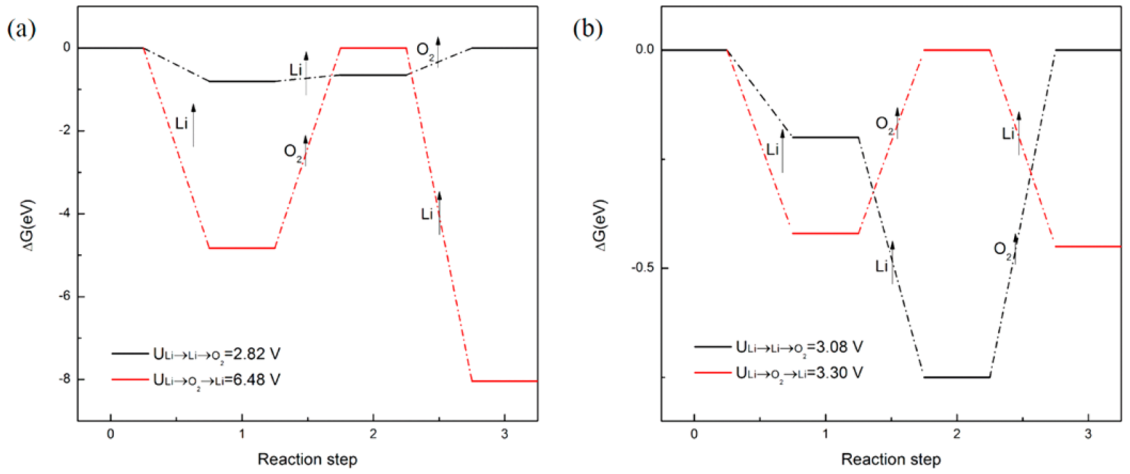

Figure 5. Energy profiles for the charge process of Li_2O_2 happened on (a) the surface of RuO_2 monolayer and (b) rutile RuO_2 {001} surface following two possible reaction routes.

batteries asymmetric. As previously mentioned, the adsorption models built above to study the initial discharge process could also be used to interpret the end stage of the charge process but obviously not the beginning and middle stages. To describe the charge process more accurately, while keep the computational efforts reasonable, we built solid−solid interface models following Zhu et al.'s[40,41] approach. The same amount of nanoscale Li_2O_2 was put onto both RuO_2 monolayer and rutile RuO_2 {001} surface, with {0001} surface of Li_2O_2 in contact with them. After geometry optimization, for the rutile RuO_2 {001} surface, the adsorbed Li_2O_2 showed a tilt to fit the large lattice mismatch, as shown in Figure S9; for RuO_2 monolayer, one of the oxygen−oxygen bonds near the interface was cleaved due to the lithium-rich termination.

According to previous studies,[56] the OER in nonaqueous lithium−oxygen batteries takes place at the three-phase interface of cathode/Li_2O_2/O_2. Thus, we chose a unit cell of Li_2O_2 near the RuO_2 monolayer or rutile RuO_2 {001} surface/Li_2O_2/electrolyte interface to study the OER mechanism. Two possible reaction routes, namely, $Li^+ \rightarrow Li^+ \rightarrow O_2$ (route 1) and $Li^+ \rightarrow O_2 \rightarrow Li^+$ (route 2) were considered accordingly. The energy profiles for these two different routes are shown in Figure 5. For RuO_2 monolayer, as shown in Figure 5a, the equilibrium voltage for route 1 is 2.82 V, much lower than that of 6.48 V for route 2. For rutile RuO_2 {001} surface, as shown in Figure 5b, the equilibrium voltage for route 1 is 3.08 V, which is quite close to the charge voltages reported in experiments[15,16] and a bit lower than that of 3.30 V for route 2. Thus, route 1 will be the preferred reaction route in both situations. The equilibrium charge voltage for RuO_2 monolayer is lower than that of rutile RuO_2 {001} surface, indicating a higher catalytic activity during the initial and middle stages of the charge process.

The geometry changes of the adsorbed Li_2O_2 along with the charge process following the route 1 are shown in Figure 6. It is quite interesting to find that for RuO_2 monolayer, as shown in Figure 6a, after the removal of one unit cell of Li_2O_2, the remaining Li_2O_2 will be attracted to move toward the RuO_2 monolayer spontaneously (the center of mass of the adsorbed Li_2O_2 moves toward the RuO_2 layer about 0.2 Å), while similar behavior cannot be observed for the rutile RuO_2 {001} surface, as shown in Figure 6b (the center of mass of the adsorbed Li_2O_2 moves away from the RuO_2 {001} surface about 0.4 Å).

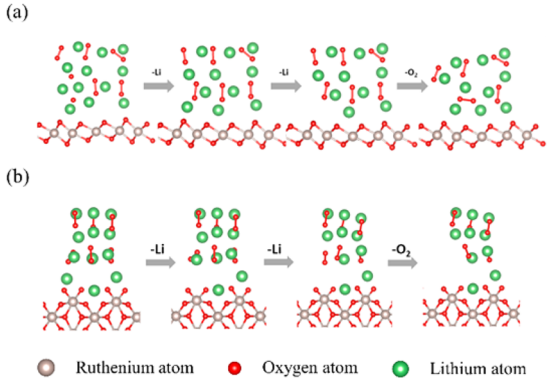

Figure 6. Geometries for the charge process following route 1 happened on (a) the surface of RuO_2 monolayer and (b) rutile RuO_2 {001} surface.

We propose that this attraction effect could help maintain the solid−solid reaction interface until all adsorbed Li_2O_2 is decomposed. Gittleson et al.[57] observed that for the gold cathode, after the beginning stage of the charge process when the first layer of Li_2O_2 was consumed, the remaining Li_2O_2 would be in poor contact with the cathode and can hardly be charged back. Our calculation results show that the vanishing of the reaction interface along with the charge process is unlikely to happen when the reactions take place on the surface of RuO_2 monolayer.

4. CONCLUSIONS

In summary, we comparatively investigated the ORR and OER in nonaqueous lithium−oxygen batteries occurring on both the surface of RuO_2 monolayer and rutile RuO_2. The calculation results show that in nonaqueous lithium−oxygen batteries, RuO_2 monolayer exhibits higher catalytic activity in both ORR and OER than rutile RuO_2 does. In addition, during discharge, the similar lattice structure between RuO_2 monolayer and Li_2O_2 {0001} can induce the conductive Li_2O_2 {0001} surface to expose, and the small lattice misfit can facilitate the electron transportation through the formation of defects or grain boundaries due to the internal strain, whereas during charge the RuO_2 monolayer can attract the adsorbed Li_2O_2 to move toward its surface to maintain the solid−solid reaction interface. Current work points out that RuO_2 monolayer is a quite

DOI: 10.1021/acs.jpcc.6b00014
J. Phys. Chem. C 2016, 120, 6356−6362

promising catalytic material for nonaqueous lithium−oxygen batteries. Further experimental and computational explorations on the application of RuO_2 monolayer as well as other cheaper 2D metal oxide materials in nonaqueous lithium−oxygen batteries are expected.

■ ASSOCIATED CONTENT

Supporting Information

The Supporting Information is available free of charge on the ACS Publications website at DOI: 10.1021/acs.jpcc.6b00014.

Optimized lattice parameters of Li_2O_2, RuO_2 monolayer, and rutile RuO_2. The orientations and terminations of rutile RuO_2 considered for the Wulff construction. Surface energies of different orientations and terminations of rutile RuO_2 under different oxygen chemical potentials. Optimized geometry for oxygen molecular adsorbed onto the surface of RuO_2 monolayer. Optimized geometry for oxygen molecular adsorbed onto rutile RuO_2 {001} surface. Optimized geometry of discharge process happened on Li_2O_2 {0001} surface with and without RuO_2 monolayer. Energy profile for the discharge process happened on the Li_2O_2 {0001} surface with and without RuO_2 monolayer. Optimized lattice parameters of Li_2O_2 before and after adsorption onto RuO_2 monolayer. Illustration for proposed formation mechanism for the assembled thin disc morphology of Li_2O_2. The geometries of the interfacial model of rutile RuO_2 {001} surface and Li_2O_2 {0001} surface before and after optimization. (PDF)

■ AUTHOR INFORMATION

Corresponding Author

*Tel: (852) 2358 8647. E-mail: metzhao@ust.hk.

Notes

The authors declare no competing financial interest.

■ ACKNOWLEDGMENTS

The work described in this paper was fully supported by a grant from the Research Grants Council of the Hong Kong Special Administrative Region, China (Project No. 16213414)

■ REFERENCES

(1) Luntz, A. C.; McCloskey, B. D. Nonaqueous Li−Air Batteries: A Status Report. *Chem. Rev.* **2014**, *114*, 11721−11750.

(2) Park, M.; Sun, H.; Lee, H.; Lee, J.; Cho, J. Lithium-Air Batteries: Survey on the Current Status and Perspectives Towards Automotive Applications from a Battery Industry Standpoint. *Adv. Energy Mater.* **2012**, *2*, 780−800.

(3) Wang, J.; Li, Y.; Sun, X. Challenges and Opportunities of Nanostructured Materials for Aprotic Rechargeable Lithium−Air Batteries. *Nano Energy* **2013**, *2*, 443−467.

(4) Peng, Z.; Freunberger, S. A.; Chen, Y.; Bruce, P. G. A Reversible and Higher-Rate Li-O_2 Battery. *Science* **2012**, *337*, 563−566.

(5) Rahman, M. A.; Wang, X.; Wen, C. A Review of High Energy Density Lithium−Air Battery Technology. *J. Appl. Electrochem.* **2014**, *44*, 5−22.

(6) Lu, Y. C.; Gallant, B. M.; Kwabi, D. G.; Harding, J. R.; Mitchell, R. R.; Whittingham, M. S.; Shao-Horn, Y. Lithium−Oxygen Batteries: Bridging Mechanistic Understanding and Battery Performance. *Energy Environ. Sci.* **2013**, *6*, 750−768.

(7) Shi, L.; Zhao, T. Why the Charge Overpotential in Non-Aqueous Li−O_2 Batteries Is So High and Exhibits Different Rising Trends? *Sci. Bull.* **2015**, *60*, 281−282.

(8) Li, F.; Zhang, T.; Zhou, H. Challenges of Non-Aqueous Li−O_2 Batteries: Electrolytes, Catalysts, and Anodes. *Energy Environ. Sci.* **2013**, *6*, 1125−1141.

(9) Xie, J.; Yao, X.; Madden, I. P.; Jiang, D. E.; Chou, L. Y.; Tsung, C. K.; Wang, D. Selective Deposition of Ru Nanoparticles on $TiSi_2$ Nanonet and Its Utilization for Li_2O_2 Formation and Decomposition. *J. Am. Chem. Soc.* **2014**, *136*, 8903−8906.

(10) Lu, J.; Cheng, L.; Lau, K. C.; Tyo, E.; Luo, X.; Wen, J.; Miller, D.; Assary, R. S.; Wang, H. H.; Redfern, P. Effect of the Size-Selective Silver Clusters on Lithium Peroxide Morphology in Lithium−Oxygen Batteries. *Nat. Commun.* **2014**, *5*, 4895.

(11) Mohamed, S. G.; Tsai, Y. Q.; Chen, C. J.; Tsai, Y. T.; Hung, T. F.; Chang, W. S.; Liu, R. S. Ternary Spinel MCo_2O_4 (M= Mn, Fe, Ni, and Zn) Porous Nanorods as Bifunctional Cathode Materials for Lithium-O_2 Batteries. *ACS Appl. Mater. Interfaces* **2015**, *7*, 12038−12046.

(12) Kwak, W. J.; Lau, K. C.; Shin, C. D.; Amine, K.; Curtiss, L. A.; Sun, Y. K. A Mo_2C/Carbon Nanotube Composite Cathode for Lithium−Oxygen Batteries with High Energy Efficiency and Long Cycle Life. *ACS Nano* **2015**, *9*, 4129−4137.

(13) Kundu, D.; Black, R.; Adams, B.; Harrison, K.; Zavadil, K. R.; Nazar, L. F. Nanostructured Metal Carbides for Aprotic Li-O_2 Batteries: New Insights into Interfacial Reactions and Cathode Stability. *J. Phys. Chem. Lett.* **2015**, *6*, 2252−2258.

(14) Wang, G.; Huang, L.; Huang, W.; Xie, J.; Du, G.; Zhang, S.; Zhu, P.; Cao, G.; Zhao, X. Nanostructured Porous RuO_2/MnO_2 as a Highly Efficient Catalyst for High-Rate Li−O_2 Batteries. *Nanoscale* **2015**, *7*, 20614−20624.

(15) Yilmaz, E.; Yogi, C.; Yamanaka, K.; Ohta, T.; Byon, H. R. Promoting Formation of Noncrystalline Li_2O_2 in the Li−O_2 Battery with RuO_2 Nanoparticles. *Nano Lett.* **2013**, *13*, 4679−4684.

(16) Jung, H. G.; Jeong, Y. S.; Park, J. B.; Sun, Y. K.; Scrosati, B.; Lee, Y. J. Ruthenium-Based Electrocatalysts Supported on Reduced Graphene Oxide for Lithium-Air Batteries. *ACS Nano* **2013**, *7*, 3532−3539.

(17) Guo, X.; Liu, P.; Han, J.; Ito, Y.; Hirata, A.; Fujita, T.; Chen, M. 3D Nanoporous Nitrogen-Doped Graphene with Encapsulated RuO_2 Nanoparticles for Li−O_2 Batteries. *Adv. Mater.* **2015**, *27*, 6137−6143.

(18) Fukuda, K.; Saida, T.; Sato, J.; Yonezawa, M.; Takasu, Y.; Sugimoto, W. Synthesis of Nanosheet Crystallites of Ruthenate with an α-$NaFeO_2$-Related Structure and Its Electrochemical Supercapacitor Property. *Inorg. Chem.* **2010**, *49*, 4391−4393.

(19) Sato, J.; Kato, H.; Kimura, M.; Fukuda, K.; Sugimoto, W. Conductivity of Ruthenate Nanosheets Prepared Via Electrostatic Self-Assembly: Characterization of Isolated Single Nanosheet Crystallite to Mono- and Multilayer Electrodes. *Langmuir* **2010**, *26*, 18049−18054.

(20) Chauvin, C.; Saida, T.; Sugimoto, W. Influence of the RuO_2 Nanosheet Content in RuO_2 Nanosheet-Pt/C Composite Toward Improved Performance of Oxygen Reduction Electrocatalysts. *J. Electrochem. Soc.* **2014**, *161*, F318−F322.

(21) Osada, M.; Sasaki, T. 2D Oxide Nanosheets: Controlled Assembly and Applications. *ECS Trans.* **2013**, *50*, 111−116.

(22) Liao, K.; Wang, X.; Sun, Y.; Tang, D.; Han, M.; He, P.; Jiang, X.; Zhang, T.; Zhou, H. An Oxygen Cathode with Stable Full Discharge−Charge Capability Based on 2D Conducting Oxide. *Energy Environ. Sci.* **2015**, *8*, 1992−1997.

(23) Gonze, X.; Beuken, J. M.; Caracas, R.; Detraux, F.; Fuchs, M.; Rignanese, G. M.; Sindic, L.; Verstraete, M.; Zerah, G.; Jollet, F.; et al. First-Principles Computation of Material Properties: the ABINIT Software Project. *Comput. Mater. Sci.* **2002**, *25*, 478−492.

(24) Gonze, X.; Amadon, B.; Anglade, P. M.; Beuken, J. M.; Bottin, F.; Boulanger, P.; Bruneval, F.; Caliste, D.; Caracas, R.; Cote, M.; et al. ABINIT: First-Principles Approach to Material and Nanosystem Properties. *Comput. Phys. Commun.* **2009**, *180*, 2582−2615.

(25) Gonze, X. A Brief Introduction to the ABINIT Software Package. *Z. Kristallogr. - Cryst. Mater.* **2005**, *220*, 558−562.

(26) Blöchl, P. E. Projector Augmented-Wave Method. *Phys. Rev. B: Condens. Matter Mater. Phys.* **1994**, *50*, 17953.

DOI: 10.1021/acs.jpcc.6b00014
J. Phys. Chem. C 2016, 120, 6356−6362

(27) Perdew, J. P.; Burke, K.; Ernzerhof, M. Generalized Gradient Approximation Made Simple. *Phys. Rev. Lett.* **1996**, *77*, 3865.
(28) Monkhorst, H. J.; Pack, J. D. Special Points for Brillouin-Zone Integrations. *Phys. Rev. B* **1976**, *13*, 5188.
(29) Bader, R. F. *Atoms in Molecules*; John Wiley & Sons, Ltd., 1990.
(30) Henkelman, G.; Arnaldsson, A.; Jónsson, H. A Fast and Robust Algorithm for Bader Decomposition of Charge Density. *Comput. Mater. Sci.* **2006**, *36*, 354−360.
(31) Heyd, J.; Scuseria, G. E.; Ernzerhof, M. Hybrid Functionals Based on a Screened Coulomb Potential. *J. Chem. Phys.* **2003**, *118*, 8207−8215.
(32) Paier, J.; Marsman, M.; Hummer, K.; Kresse, G.; Gerber, I. C.; Ángyán, J. G. Screened Hybrid Density Functionals Applied to Solids. *J. Chem. Phys.* **2006**, *124*, 154709.
(33) Giannozzi, P.; Baroni, S.; Bonini, N.; Calandra, M.; Car, R.; Cavazzoni, C.; Ceresoli, D.; Chiarotti, G. L.; Cococcioni, M.; Dabo, I.; et al. QUANTUM ESPRESSO: A Modular and Open-Source Software Project for Quantum Simulations of Materials. *J. Phys.: Condens. Matter* **2009**, *21*, 395502.
(34) Shikano, M.; Delmas, C.; Darriet, J. $NaRuO_2$ and $Na_xRuO_2{\bullet}yH_2O$: New Oxide and Oxyhydrate with Two Dimensional RuO_2 Layers. *Inorg. Chem.* **2004**, *43*, 1214−1216.
(35) Baur, W. H.; Khan, A. A. Rutile-Type Compounds. IV. SiO_2, GeO_2 and a Comparison with Other Rutile-Type Structures. *Acta Crystallogr., Sect. B: Struct. Crystallogr. Cryst. Chem.* **1971**, *27*, 2133−2139.
(36) Cota, L. G.; de la Mora, P. On the Structure of Lithium Peroxide, Li_2O_2. *Acta Crystallogr., Sect. B: Struct. Sci.* **2005**, *61*, 133−136.
(37) Kaminsky, W. WinXMorph: A Computer Program to Draw Crystal Morphology, Growth Sectors and Cross Sections with Export Files in VRML V2.0 utf8-virtual Reality Format. *J. Appl. Crystallogr.* **2005**, *38*, 566−567.
(38) Radin, M. D.; Rodriguez, J. F.; Tian, F.; Siegel, D. J. Lithium Peroxide Surfaces Are Metallic, While Lithium Oxide Surfaces Are Not. *J. Am. Chem. Soc.* **2012**, *134*, 1093−1103.
(39) Stull, D. R.; Prophet, H. *JANAF Thermochemical Tables*; National Standard Reference Data System, 1971.
(40) Zhu, J.; Ren, X.; Liu, J.; Zhang, W.; Wen, Z. Unraveling the Catalytic Mechanism of Co_3O_4 for the Oxygen Evolution Reaction in a Li−O_2 Battery. *ACS Catal.* **2015**, *5*, 73−81.
(41) Zhu, J.; Wang, F.; Wang, B.; Wang, Y.; Liu, J.; Zhang, W.; Wen, Z. Surface Acidity as Descriptor of Catalytic Activity for Oxygen Evolution Reaction in Li-O_2 Battery. *J. Am. Chem. Soc.* **2015**, *137*, 13572−13579.
(42) Mo, Y.; Ong, S. P.; Ceder, G. First-principles Study of the Oxygen Evolution Reaction of Lithium Peroxide in the Lithium-Air battery. *Phys. Rev. B: Condens. Matter Mater. Phys.* **2011**, *84*, 205446.
(43) Zhai, D.; Wang, H. H.; Yang, J.; Lau, K. C.; Li, K.; Amine, K.; Curtiss, L. A. Disproportionation in Li−O_2 Batteries Based on a Large Surface Area Carbon Cathode. *J. Am. Chem. Soc.* **2013**, *135*, 15364−15372.
(44) Johnson, L.; Li, C.; Liu, Z.; Chen, Y.; Freunberger, S. A.; Ashok, P. C.; Praveen, B. B.; Dholakia, K.; Tarascon, J. M.; Bruce, P. G. The Role of LiO_2 Solubility in O_2 Reduction in Aprotic Solvents and Its Consequences for Li−O_2 Batteries.". *Nat. Chem.* **2014**, *6*, 1091−1099.
(45) Geng, W. T.; Ohno, T. Li_2O_2 Wetting on the (110) Surface of RuO_2, TiO_2, and SnO_2: An Initiating Force for Polycrystalline Growth. *J. Phys. Chem. C* **2015**, *119*, 1024−1031.
(46) Tan, P.; Shi, L.; Shyy, W.; Zhao, T. S. Morphology of the Discharge Product in Non-Aqueous Lithium-Oxygen Batteries: Furrowed Toroid Particles Correspond to a Higher Energy Efficiency. *Energy Technol.* **2016**, *4*, 393.
(47) Shi, L.; Xu, A.; Zhao, T. S. Formation of Li_3O_4 Nano Particles in the Discharge Products of Non-Aqueous Lithium−Oxygen Batteries Leads to Lower Charge Overvoltage. *Phys. Chem. Chem. Phys.* **2015**, *17*, 29859−29866.
(48) Viswanathan, V.; Thygesen, K. S.; Hummelshøj, J. S.; Nørskov, J. K.; Girishkumar, G.; McCloskey, B. D.; Luntz, A. C. Electrical Conductivity in Li_2O_2 and Its Role in Determining Capacity Limitations in Non-Aqueous Li-O_2 Batteries. *J. Chem. Phys.* **2011**, *135*, 214704.
(49) Hummelshøj, J. S.; Blomqvist, J.; Datta, S.; Vegge, T.; Rossmeisl, J.; Thygesen, K. S.; Luntz, A. C.; Jacobsen, K. W.; Nørskov, J. K. Communications: Elementary Oxygen Electrode Reactions in the Aprotic Li-air Battery. *J. Chem. Phys.* **2010**, *132*, 071101.
(50) Brune, H.; Kern, K. *Growth and Properties of Ultrathin Epitaxial Layers*; Elsevier, 1997.
(51) Geng, W. T.; He, B. L.; Ohno, T. Grain Boundary Induced Conductivity in Li_2O_2. *J. Phys. Chem. C* **2013**, *117*, 25222−25228.
(52) Wang, Z.; Sun, J.; Cheng, Y.; Niu, C. Adsorption and Deposition of Li_2O_2 on TiC {111} Surface. *J. Phys. Chem. Lett.* **2014**, *5*, 3919−3923.
(53) Ottakam Thotiyl, M. M.; Freunberger, S. A.; Peng, Z.; Chen, Y.; Liu, Z.; Bruce, P. G. A Stable Cathode for the Aprotic Li−O_2 Battery. *Nat. Mater.* **2013**, *12*, 1050−1056.
(54) Tersoff, J.; LeGoues, F. K. Competing Relaxation Mechanisms in Strained Layers. *Phys. Rev. Lett.* **1994**, *72*, 3570.
(55) Obraztsov, A. N.; Obraztsova, E. A.; Tyurnina, A. V.; Zolotukhin, A. A. Chemical Vapor Deposition of Thin Graphite Films of Nanometer Thickness. *Carbon* **2007**, *45*, 2017−2021.
(56) Zhong, L.; Mitchell, R. R.; Liu, Y.; Gallant, B. M.; Thompson, C. V.; Huang, J. Y.; Mao, S. X.; Shao-Horn, Y. In situ Transmission Electron Microscopy Observations of Electrochemical Oxidation of Li_2O_2. *Nano Lett.* **2013**, *13*, 2209−2214.
(57) Gittleson, F. S.; Ryu, W. H.; Taylor, A. D. Operando Observation of the Gold−Electrolyte Interface in Li−O_2 Batteries. *ACS Appl. Mater. Interfaces* **2014**, *6*, 19017−19025.

DOI: 10.1021/acs.jpcc.6b00014
J. Phys. Chem. C 2016, 120, 6356−6362